Dynamics of a strongly interacting Fermi gas: The radial quadrupole mode

A. Altmeyer,[1] S. Riedl,[1,2] M. J. Wright,[1] C. Kohstall,[1] J. Hecker Denschlag,[1] and R. Grimm[1,2]
[1]*Institute of Experimental Physics and Center for Quantum Physics, University of Innsbruck, 6020 Innsbruck, Austria*
[2]*Institute for Quantum Optics and Quantum Information, Austrian Academy of Sciences, 6020 Innsbruck, Austria*
(Received 25 April 2007; published 18 September 2007)

We report on measurements of an elementary surface mode in an ultracold, strongly interacting Fermi gas of ^{6}Li atoms. The radial quadrupole mode allows us to probe hydrodynamic behavior in the crossover from Bose-Einstein condensation (BEC) to the Bardeen-Cooper-Schrieffer (BCS) regime without being influenced by changes in the equation of state. We examine the frequency and damping of this mode, along with its expansion dynamics. In the unitarity limit and on the BEC side of the resonance, the observed frequencies agree with standard hydrodynamic theory. However, on the BCS side of the crossover, a striking downshift of the oscillation frequency is observed in the hydrodynamic regime as a precursor to an abrupt transition to collisionless behavior; this indicates coupling of the oscillation to fermionic pairs.

DOI: 10.1103/PhysRevA.76.033610 PACS number(s): 03.75.Ss, 34.50.−s, 05.30.Fk, 39.25.+k

I. INTRODUCTION

The advent of ultracold, strongly interacting Fermi gases [1,2], molecular Bose-Einstein condensates [3–5], and fermionic condensates [6,7] has opened up unique possibilities to study the fundamental physics of interacting fermions. The availability of controllable model systems with tunable interactions provides unprecedented experimental access to the many-body physics of fermionic quantum systems, which is of great fundamental importance for various branches of physics [8].

A fundamental problem, which has been discussed in the theoretical literature for decades [9–12], is the crossover from Bose-Einstein condensation (BEC) to a macroscopic quantum state in the Bardeen-Cooper-Schrieffer (BCS) regime. In this crossover, the nature of pairing changes from the formation of bosonic molecules by fermionic atoms to pairing supported by many-body effects. With novel model systems now available in ultracold Fermi gases, the BEC-BCS crossover has recently stimulated a great deal of interest in both theory and experiment [8].

Collective excitation modes in trapped ultracold Fermi gases provide powerful tools to investigate the macroscopic properties of a system in the BEC-BCS crossover [13]. For experiments of this class, ultracold ^{6}Li gases have excellent properties. This is because of their stability in the molecular regime [3,14,15] and precise magnetic tunability of interactions based on a broad Feshbach resonance [16,17]. Early experiments on collective modes in the BEC-BCS crossover provided evidence for superfluidity [18] and showed a striking transition from hydrodynamic to collisionless behavior [19]. More recent experiments yielded a precision test of the equation of state [20]. The previous experiments have focused on collective modes with compression character, where both the hydrodynamic properties and the equation of state determine the mode frequency [18–23].

In this article, we report on measurements of a *pure surface mode* in the BEC-BCS crossover, which provides insight into the dynamics of the system. The "radial quadrupole mode" in an elongated trap, the fundamentals of which are discussed in Sec. II, allows for a test of hydrodynamic behavior without being influenced by changes in the equation of state. In Sec. III, we present our experimental setup and the main procedures. We introduce a tool to excite collective oscillations with an acousto-optic scanning system. The results of our measurements, presented in Sec. IV, provide us with insight into the abrupt transition from hydrodynamic to collisionless behavior, first observed in [19]. The present work provides strong evidence that quasistatic hydrodynamic theory [24] does not apply to collective modes of a strongly interacting fermionic superfluid, when the oscillation frequencies approach the pairing gap [25].

II. RADIAL QUADRUPOLE MODE

The confining potential in our experiments is close to the limit of an elongated harmonic trap with cylindrical symmetry. In this case, we can consider purely radial collective oscillations, neglecting the axial motion. The frequencies of the radial modes can be expressed in units of the radial trap frequency ω_r. We note that our experiments are performed in a three-dimensional regime, where the energy $\hbar\omega_r$ is typically a factor of 30 below the chemical potential and finite-size effects can be neglected.

In this situation, there are two elementary collective modes of the system: the radial compression mode and the radial quadrupole mode [13,26]. We focus on the quadrupole mode, which is illustrated in Fig. 1. This mode corresponds to an oscillating radial deformation, which can be interpreted as a standing surface wave. The mode was first demonstrated in atomic BEC experiments [27] and applied to investigate rotating systems [28], but so far it has not been studied in strongly interacting Fermi gases.

Being a pure surface mode, the frequency ω_q of the radial quadrupole mode does not depend on the compressibility of the system. The frequency ω_q does not depend on the equation of state but on the collisional properties. In the hydrodynamic regime, whether the gas is a superfluid or a classical gas with a collision rate strongly exceeding the radial trap frequency, the frequency of this mode is given by [26]

$$\omega_q = \sqrt{2}\omega_r. \tag{1}$$

In contrast, for a collisionless gas, where the atoms freely oscillate in the trap, the frequency is

 ©2007 The American Physical Society

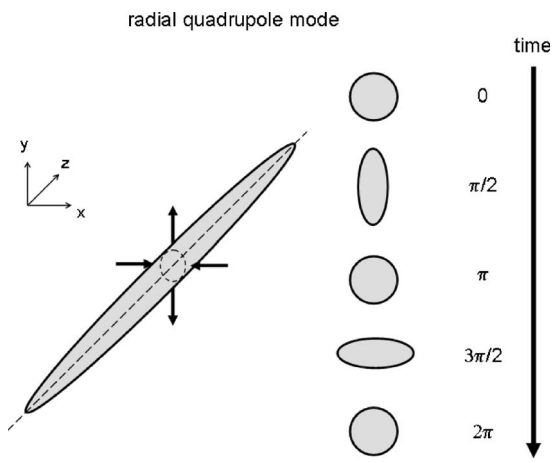

FIG. 1. Illustration of the radial quadrupole mode as an elementary collective excitation of an elongated, trapped atom cloud.

$$\omega_q = 2\omega_r. \tag{2}$$

Because ω_q is insensitive to the compressibility of the gas and the difference between the collisionless and the hydrodynamic frequencies is large, the radial quadrupole mode can serve as an excellent tool to probe pure hydrodynamics. Particularly interesting is the transition from hydrodynamic to collisionless behavior at the lowest temperatures. Such a change occurs in a strongly interacting Fermi gas on the BCS side of the resonance [19,21,23]. Near this transition, measurements on the compression mode indicated frequency downshifts, which raised questions concerning the validity of standard hydrodynamic theory in this interaction regime [29,30]. Previous experiments could not unambiguously identify the origin of frequency shifts near the hydrodynamic-to-collisionless transition, which is a particular motivation for probing the crossover gas with the radial quadrupole mode.

III. EXPERIMENTAL PROCEDURE

The apparatus and the basic preparation methods for experiments with a strongly interacting Fermi gas of ^{6}Li atoms have been described in our previous work [3,19,25,31]. As a starting point, we produce a molecular BEC of $^6Li_2$ [3,31]. By changing an external magnetic field, we can control the interparticle interactions in the vicinity of a Feshbach resonance, which is centered at 834 G [16,17]. The interactions are characterized by the atomic *s*-wave scattering length a.

We start our experiments with an ensemble of about $N = 4 \times 10^5$ atoms in an almost pure BEC at a magnetic field of 764 G. In order to change the properties of the system adiabatically, we slowly ramp to the final magnetic field, where the measurements are performed [31]. The temperature of the gas is typically below 0.1 T_F, unless stated otherwise.

In order to observe the collective oscillations, we take absorption images of the cloud in the *x*-*y* plane after release from the trap. We illuminate the atoms with a probe beam along the z direction of the cigar-shaped cloud. The probe light causes a resonant excitation of the D2 line at a wavelength of 671 nm. We use dichroic mirrors for combining and separating the probe and the dipole-trapping beam. The frequency of the probe beam can be tuned over a range of more than 1 GHz, which enables resonant imaging over the whole range of magnetic fields that we create in our experiments.

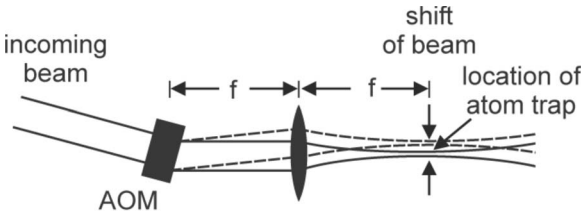

FIG. 2. Schematic illustration of the scanning system. A wide collimated beam passes through an AOM. The resulting deflection angle depends on the driving frequency of the AOM. The beam passes through a lens at the distance of one focal length behind the AOM. The lens focuses the beam for atom trapping. A change in deflection angle results in a parallel shift of the beam position in the focal plane. The solid and dashed lines show the beam path for different deflection angles. The zeroth-order beam is not shown.

The gas is confined in a nearly harmonic trapping potential, which has an axially symmetric, cigar-shaped trap geometry. Optical confinement in the radial direction is created by a focused 1030-nm near-infrared laser beam with a waist of ~ 58 μm. The potential in the axial direction consists of a combination of optical and magnetic confinement [3]; the magnetic confinement is dominant under the conditions of the present experiments. We set the laser power to 270 mW, which results in a radial trap frequency of $\omega_r \approx 2\pi \times 370$ Hz and an axial trap frequency of $\omega_z \approx 2\pi \times 22$ Hz at a magnetic field of 764 G. The trap frequencies correspond to the Fermi energy of a noninteracting cloud, $E_F = \hbar(\omega_r^2 \omega_z 3N)^{1/3} = k_B \times 740$ nK.

In order to excite collective oscillations, we suddenly change the optical trapping potential. The position and shape of our trapping potential in the *x*-*y* plane can be manipulated through the use of a two-dimensional scanning system. One feature of the system is that we can rapidly displace the trap laterally. Fast modulation of the beam position enables us to create time-averaged potentials [32,33].

The scanning system is constructed by use of two acousto-optic modulators (AOMs), which are aligned for vertical and horizontal deflections. Figure 2 illustrates the principle of our scanning system for one direction. A collimated beam passes through an AOM and is deflected depending on the driving frequency. A lens is placed at a distance of one focal length behind the AOM, so that the deflection results in a parallel displacement of the beam. By changing the driving frequency of the AOM, the lateral position of the focus is shifted. This system enables us to displace the focus of the trapping beam in the horizontal and the vertical direction by up to 4 times the beam waist in all directions. Furthermore, the deflection can be modulated by frequencies of up to ~ 1 MHz within 3 dB bandwidth. In our trap configuration, we use modulation frequencies of 100 kHz, which greatly exceeds the trap frequency. We create elliptic potentials—i.e., potentials with $\omega_x \neq \omega_y$—by

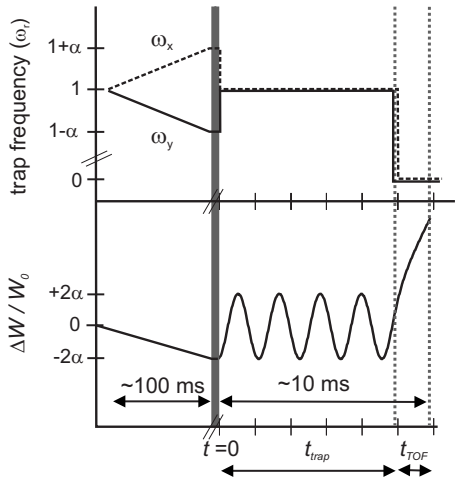

FIG. 3. Timing scheme for the excitation of the radial quadrupole mode. The ellipticity of the trap is slowly ramped up within 100 ms. This results in a change of α in the trap frequencies, where α characterizes the ellipticity and sets the initial, normalized deformation $\Delta W/W_0=-2\alpha$. W_0 is defined as the width of the cloud in the trap without excitation. At $t=0$, the elliptic deformation is switched off and the oscillation in the trap begins. (Shown here is an oscillation in the hydrodynamic regime.) The oscillation continues until the trap is turned off at $t=t_{\mathrm{trap}}$, which is usually between 0 and 10 ms. At $t=t_{\mathrm{trap}}$, the cloud is released from the trap and expands for the time t_{TOF}, which is typically 2 ms.

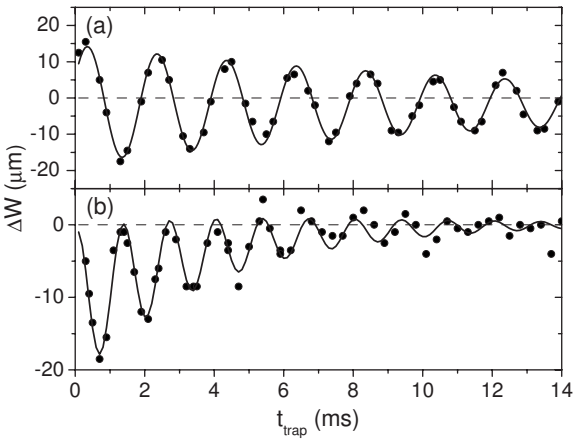

FIG. 4. Typical radial quadrupole oscillations in the hydrodynamic (a) and collisionless (b) regimes. The solid lines show fits to our data according to Eq. (3). The dashed lines indicate $\Delta W=0$. The expansion time t_{TOF} is 2 ms. In (a), the oscillation in the unitarity limit ($B=834$ G) is shown, whereas (b) shows the oscillations for $B=1132$ G ($1/k_{\mathrm{F}}a\approx-1.34$).

modulating the trap position along a specific direction. We use this for the excitation of the quadrupole mode. By choosing a suited modulation function [34], these elliptic potentials are nearly harmonic.

When we excite the quadrupole mode, we first adiabatically deform the trapping potential in ~100 ms to an elliptic shape. This slow deformation ensures that the cloud stays in thermal equilibrium even in the near-collisionless regime and no excitations occur. We suddenly switch off the deformation, leading to an oscillation in the x-y plane of the elliptic cloud in the originally round trap.

The initial deformation corresponds to different trap frequencies in the horizontal and vertical directions where $\omega_{0x}=(1+\alpha)\omega_{\mathrm{r}}$ and $\omega_{0y}=(1-\alpha)\omega_{\mathrm{r}}$. The parameter α determines the amplitude of the emerging oscillation; we choose it for most of our measurements (unless stated otherwise) to be $\alpha\approx0.05$. We increase α by increasing the modulation for the time averaged potential along the y direction. As the modulation decreases the confinement strength of the dipole trap, we simultaneously ramp up the trap power to ensure that the mean trap frequency $\omega_{\mathrm{r}}=\sqrt{\omega_{0x}\omega_{0y}}$ remains constant. This avoids excitation of the compression mode.

Figure 3 shows the timing scheme for the excitation of the radial quadrupole mode. At $t=0$, the collective oscillation is excited and the cloud starts oscillating in the trap for a variable time t_{trap}. Horizontal and vertical widths of the cloud, W_x and W_y, oscillate in the trap out of phase with a relative phase shift of π. As an observable, we choose the difference in the widths, $\Delta W=W_x-W_y$, which cancels out small effects of residual compression oscillations. For normalization, we introduce the width W_0 of the cloud in the trap without excitation.

Experimentally, we determine the collective quadrupole oscillations after suddenly switching off the trap and a subsequent expansion time t_{TOF}. We then take an absorption image of the cloud and determine its horizontal and vertical widths W_x and W_y via a two-dimensional Thomas-Fermi profile fit. From these measurements after expansion, we can determine the in-trap behavior.

Typical data sets of radial quadrupole oscillations are shown in Fig. 4. Figure 4(a) shows an oscillation in the hydrodynamic regime; here, we observe a weakly damped harmonic oscillation centered about a small constant offset. Figure 4(b) shows the typical behavior in the collisionless regime. The frequency of the oscillation is clearly higher than in the hydrodynamic regime. The oscillation shows stronger damping and has an exponentially time-varying offset.

We find that, for both regimes, the dependence of ΔW on t_{trap} can be well described by the fit function

$$\Delta W = Ae^{-\kappa t_{\mathrm{trap}}}\cos(\omega_{\mathrm{q}}t_{\mathrm{trap}}+\phi)+Ce^{-\xi t_{\mathrm{trap}}}+y_0, \qquad (3)$$

which is explained in detail in Appendix B.

Note that the frequency ω_{q} and the damping constant κ are independent of the expansion during t_{TOF} and characterize the behavior of the trapped oscillating atom cloud. In contrast, the amplitude A and the phase shift ϕ depend on the expansion time and provide further information on the dynamics of the gas. The offset function $Ce^{-\xi t_{\mathrm{trap}}}$ with amplitude C and damping constant ξ results from thermalization effects and is only relevant in the collisionless regime (see discussion in Appendix B). The constant offset y_0 results from a slight inhomogeneity of the magnetic field, which gives rise to a weak saddle potential. This increases (decreases) the cloud size in the y direction (x direction) during expansion.

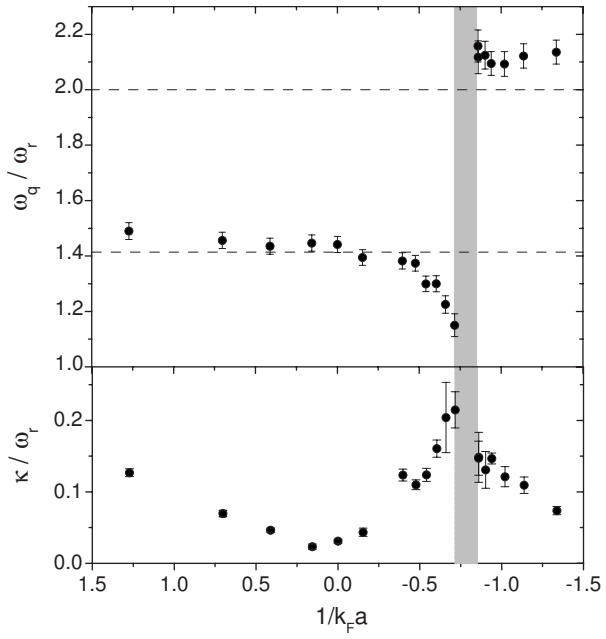

FIG. 5. Frequency ω_q (upper plot) and damping rate κ (lower plot) of the radial quadrupole mode. Both quantities are normalized to the radial trap frequency ω_r and plotted versus the interaction parameter $1/k_F a$. The dashed lines indicate the theoretical predictions in the hydrodynamic ($\omega_q/\omega_r=\sqrt{2}$) and in the collisionless limit ($\omega_q/\omega_r=2$). The shaded area marks the transition from hydrodynamic to collisionless behavior between $1/k_F a \approx -0.72$ ($B \approx 930$ G) and $1/k_F a \approx -0.85$ ($B \approx 960$ G).

IV. EXPERIMENTAL RESULTS

Here we first discuss our measurements of the frequency ω_q and the damping rate κ of the in-trap oscillation (Sec. IV A). We then present the data for the phase offset ϕ and the amplitude A (Sec. IV B). Finally, we explore the hydrodynamic-to-collisionless transition (Sec. IV C). As commonly used in the field of BEC-BCS crossover physics [8], the dimensionless parameter $1/k_F a$ is introduced to characterize the interaction regime. The parameter $k_F = \sqrt{2mE_F}/\hbar$ is the Fermi wave number and m is the mass of an atom.

A. Frequency and damping

In Fig. 5, we show the results for the frequency ω_q and the damping rate κ of the radial quadrupole mode throughout the BEC-BCS crossover. Both ω_q and κ are normalized to the trap frequency ω_r, which we determine by a sloshing mode measurement [20]. We include small corrections resulting from anharmonicity of the trapping potential and the residual ellipticity of the trap (see Appendix C).

The data confirm the expected transition between the hydrodynamic and the collisionless regime on the BCS side of the resonance (see Sec. II). The transition is qualitatively different from the hydrodynamic-to-collisionless crossover in a classical gas [35] or in a Fermi gas without superfluidity [36]. Instead of a continuous and monotonous variation of the frequency between the two limits ($\sqrt{2}\omega_r$ and $2\omega_r$), an abrupt change occurs. When this transition is approached from the hydrodynamic side, a striking frequency downshift shows up as a precursor of the transition to higher frequencies. In the transition region (shaded area in Fig. 5), no data points are shown because of the large damping and correspondingly very large uncertainties for the measured frequency.

The damping rate shows similar behavior as in our previous measurements on the radial compression mode [19,23]. Maximum damping occurs near the hydrodynamic-to-collisionless transition, whereas minimum damping is observed slightly below the resonance. In general, we find that damping is roughly 2 times larger for the quadrupole mode than for the compression mode at the same temperature [37]. The faster damping of the quadrupole mode is plausible in view of the larger frequency change at the transition. We now discuss the behavior in different regions in more detail.

$1/k_F a \approx 0$. In the unitarity limit, the normalized frequency agrees well with the theoretically expected value of $\omega_q/\omega_r = \sqrt{2}$ for a hydrodynamic gas; see Eq. (1). To check for consistency with previous experiments [20], we here also reproduced the frequency $\sqrt{10/3}\omega_r$ of the radial compression mode on a 10^{-3} accuracy level. The damping is low for the Fermi gas in the unitarity limit. In contrast to the compression mode, the quadrupole-mode frequency stays constant throughout the crossover, indicating that it is independent of the equation of state.

$1/k_F a > 0$. In the strongly interacting BEC regime, there is an increase in the damping and a slight increase in the frequency for increasing $1/k_F a$. As the gas is more susceptible to heating by inelastic processes in the deep molecular regime [13], both effects may be due to a thermal component in this region.

$1/k_F a \approx -0.8$. The frequency exhibits a pronounced "jump" from the hydrodynamic to the collisionless frequency. This transition is accompanied by a pronounced maximum of the damping rate.

$1/k_F a \lesssim -0.8$. The frequency stays almost constant about 5% above the theoretically expected value of $\omega_q = 2\omega_r$. Interaction effects in the attractive Fermi gas are likely to cause this significant upshift [38,39]. As we cannot experimentally realize a noninteracting Fermi gas above the resonance, we could not perform further experimental checks.

$1/k_F a \lesssim 0$ and $1/k_F a \gtrsim -0.8$. In this regime, we detect a substantial downshift in the quadrupole-mode frequency. The effect begins to show up already slightly above the resonance ($1/k_F a = 0$) and increases to a magnitude of almost 20% ($\omega_q/\omega_r \approx 1.15$ at $1/k_F a = -0.72$), before the transition to collisionless behavior occurs. Indications of a similar downshift have been observed already in compression-mode experiments [19,21,23], but here the downshift is considerably larger and not blurred by changes in the equation of state.

A plausible explanation for the curious behavior of the collective-mode frequency on the BCS side of the resonance is provided by coupling of the oscillation to the pairing gap [13,25,29]. If we assume that the abrupt transition is caused by pair breaking resulting from resonant coupling of the oscillation to the gap, then the downshift may be interpreted as a coupling effect when the gap is not much larger than the oscillation frequency [30]. A similar shift may also arise

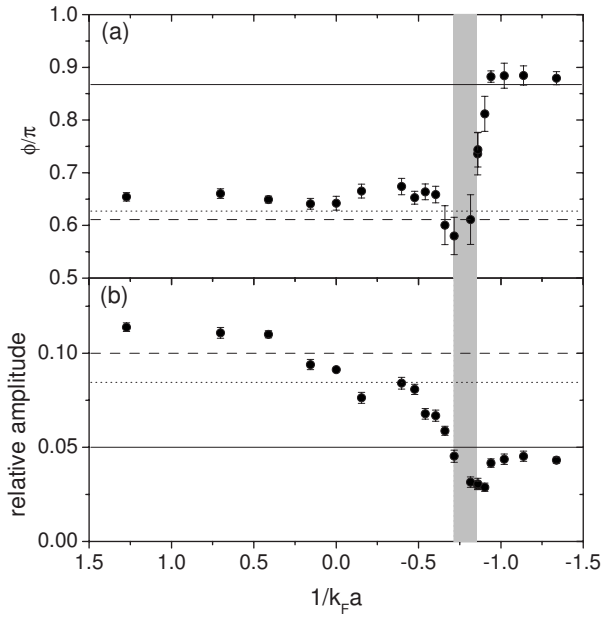

FIG. 6. (a) Phase shift ϕ and (b) relative amplitude of the quadrupole mode versus interaction parameter $1/k_F a$ after $t_{TOF}=2$ ms expansion. The horizontal lines show calculations from our theoretical model: the solid lines in the collisionless limit, the dotted lines in the hydrodynamic regime at unitarity ($\gamma=2/3$), and the dashed lines in the hydrodynamic regime in the BEC limit ($\gamma=1$). These calculated values can be read off from Fig. 10 for the phase and Fig. 9 for the amplitude. The shaded area marks the transition between hydrodynamic and collisionless behavior between $1/k_F a \approx -0.72$ and $1/k_F a \approx -0.85$ (see also Fig. 5).

from coupling of hydrodynamics and quasiparticle motion [39]. The observed phenomenon still awaits a full theoretical interpretation.

B. Phase shift and amplitude

Additional information on the interaction regime is provided by the phase shift ϕ and the amplitude A of the observed oscillation [see Eq. (3)]. This is useful since extremely high damping in the transition region makes a meaningful determination of frequency and damping practically impossible. We find that both the amplitude and phase shift, however, can be determined with reasonable uncertainties even in the transition regime.

In the following, we present measurements of the phase shift and amplitude. These are compared to model calculations, which are described in detail in Appendix A.

In Fig. 6, the phase ϕ and the relative amplitude are plotted versus the interaction parameter $1/k_F a$. The relative amplitude is given by the amplitude A [for a definition, see Eq. (3)] divided by the average width of the cloud after expansion. The average width is obtained by averaging $(W_x+W_y)/2$ over one oscillation period using the same data set from which we extract A.

In the transition area around $1/k_F a=-0.8$, the phase shift ϕ shows a steplike change at the transition from the hydrodynamic to the collisionless regime. This is similar to the jump in frequency in Fig. 5. In the collisionless and unitary regimes, the phase agrees with the theoretically expected values (solid line and dotted line, respectively).

As a general trend, the relative amplitude is larger in the hydrodynamic and smaller in the collisionless regime. In the hydrodynamic regime, the relative amplitude decreases for decreasing $1/k_F a$, which is explained by the change of γ from 1 to 2/3; γ is the polytropic index of the equation of state (see Appendix A). At unitarity, the relative amplitude agrees well with the numerically calculated value for $\gamma=2/3$ (dotted line). In the collisionless limit, the relative amplitude is half of the value at unitarity, which is also consistent with our calculations in Appendix C. We note that at the transition from the hydrodynamic to the collisionless regime, the value of the relative amplitude decreases even below the collisionless value.

In summary, the behavior of the phase shift and the amplitude agrees with our model presented in Appendix A (see also Figs. 9 and 10); in particular, the prominent change in the phase offset is confirmed.

C. Further observations

The measurements presented in the preceding subsections were taken under fixed experimental conditions, where only the scattering length a was varied. In this subsection we investigate how the transition from hydrodynamic to collisionless behavior depends on the experimental parameters excitation amplitude, trap depth, and temperature.

In a first set of experiments, we explored whether the position of the transition depends on the excitation amplitude. We increase or decrease the amplitude by a factor of 2. This allows us to compare the oscillations where the amplitude is ~20%, ~10%, and ~5% of the averaged width. We do not observe any significant change in the position of the transition.

In general, we find that the transition always occurs when the mode frequency is similar to the pairing gap. This is supported by the fact that when we vary the trap depth the transition occurs at a constant scattering length ($a \approx -5000 a_0$, $B \approx 960$ G) and does not depend on $1/k_F a$ [40]. A change in laser power of our trapping laser influences both the Fermi energy E_F and the frequency ω_q. As we increase the trap power by a factor of 10, we also increase the radial trap frequencies by a factor of $\sqrt{10} \approx 3.2$. This changes the Fermi energy by a factor of 2.2 and the pairing gap, which scales like the trap frequencies, by roughly a factor of 3 [25]. These findings suggest that the transition is linked to a coupling of the collective oscillation to the pairing gap. This is also in agreement with earlier results on the radial compression mode [13,19].

To explore the temperature dependence of the transition between the hydrodynamic and collisionless phases, we use a controlled heating scheme similar to the one described in [20], where we hold the gas in a recompressed trap and let it heat up. We set the magnetic field to 920 G ($1/k_F a=-0.66$)—i.e., slightly below the hydrodynamic-to-collisionless transition, where the regime is still clearly hydrodynamic. We observe the oscillations in a gas at the lowest temperature we can achieve in our experiments (solid

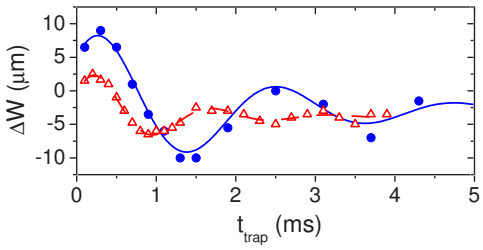

FIG. 7. (Color online) Oscillations of the quadrupole surface mode at a magnetic field of 920 G and $1/k_F a=-0.66$. The solid circles correspond to a cold ensemble, whereas the open triangles correspond to a heated ensemble. The solid lines are fits to the data according to Eq. (3).

circles) and in a "hotter" gas (open triangles) in Fig. 7. The temperature of the cold gas is $\lesssim 0.1T_F$, and we believe the temperature of the heated gas to be $\lesssim 0.2T_F$. Figure 7 clearly shows that the frequency for the colder ensemble is lower than that of the heated one and the amplitude is lower by roughly a factor of 2. Using our model in Appendix A this indicates a temperature-driven transfer of the ensemble from the hydrodynamic to the collisionless regime.

Thus we find that the radial quadrupole mode is suited to detect temperature-induced changes of the collisional regime of the gas. An exploration of the phase diagram of our system depending on temperature is possible, but beyond the scope of this article. In our laboratory, work is currently in progress on the radial scissors mode, which turns out to be an even better tool for the exploration of temperature effects.

V. CONCLUSIONS

We have presented measurements on the radial quadrupole mode of an ultracold ^{6}Li Fermi gas in the BEC-BCS crossover. As a pure surface excitation, this elementary mode probes hydrodynamic behavior without being affected by changes in the equation of state. We have measured the characteristic properties of this collective mode in a wide range of interaction strengths.

Our observations provide insight into the dynamics of the gas, in particular on the BCS side of the crossover, where the character of the oscillations abruptly changes from hydrodynamic to collisionless behavior. Our measurements presented in this paper show the phenomenon much clearer than in the radial compression mode [19,21,23] and provide quantitative data on the behavior near the transition. In particular, the data show that a substantial downshift of the collective-mode frequency occurs in the hydrodynamic regime as a precursor of the transition.

The experimental results support the interpretation that the coupling of oscillation mode and pairing gap [13,25,29] plays a crucial role for the collective excitation dynamics on the BCS side of the crossover. We anticipate that our quantitative data on the hydrodynamic-to-collisionless transition will stimulate further theoretical investigations of this intriguing phenomenon.

ACKNOWLEDGMENTS

We thank S. Stringari and M. Urban for stimulating discussions. We thank E. R. Sánchez Guajardo for helpful discussions during the process of writing this paper. We acknowledge support by the Austrian Science Fund (FWF) within SFB 15 (project part 21). S.R. is supported within the Doktorandenprogramm of the Austrian Academy of Sciences. M.J.W. is supported by a Marie Curie grant within the 6th European Community Framework Program (40333).

APPENDIX A: SCALING APPROACH AND EXPANSION EFFECTS

Here we present a theoretical model to describe the oscillation of the cloud in the trap as well as its expansion after release; the model adopts the scaling approach applied in [41–43]. The interplay between the dynamics of the collective mode and the expansion behavior is of particular interest as it introduces novel methods to investigate the collisional regime. We use a scaling approach for both the hydrodynamic and the collisionless regime [41–43]. In Appendix A 1, the limit of a hydrodynamic gas is presented, whereas in Appendix A 2, the model in the collisionless regime is discussed. Based on these models, we show calculated results for the amplitude and the phase after expansion in Appendix A 3.

The scaling approach describes the cloud at the time t after excitation [41–43]. Using the scaling function $b_i(t)$ for $i=x,y$, the width $W_i(t)$ for all times $t>0$ can be written as

$$W_i(t) = b_i(t)W_i(0), 1 \tag{A1}$$

where $W_x(0)=(1-\alpha)W_0$ and $W_y(0)=(1+\alpha)W_0$ are the initial widths at excitation and W_0 is the width of the cloud without excitation. The initial conditions for the scaling function are $b_i(0)=1$ and $\dot{b}_i(0)=0$.

1. Dynamic behavior in the hydrodynamic limit

In the hydrodynamic limit, the equations of hydrodynamics lead to the following differential equations for b_x and b_y [42]:

$$\ddot{b}_x = \frac{\omega_{0x}^2}{b_x(b_x b_y)^\gamma} - b_x\omega_x^2,$$

$$\ddot{b}_y = \frac{\omega_{0y}^2}{b_y(b_x b_y)^\gamma} - b_y\omega_y^2, \tag{A2}$$

where γ is the polytropic index of the equation of state and $b_z(t)=1$ for our elongated trap geometry. The parameters ω_{0x} and ω_{0y} are the trap frequencies at the moment of excitation ($t=0$) when the cloud has no further excitation and is in thermal equilibrium. In contrast to this, $\omega_x(t)$ and $\omega_y(t)$ are the time-dependent trap frequencies. The timing scheme is illustrated in Fig. 3. The following equation summarizes the behavior of the trap frequencies $\omega_i(t)$:

$$\omega_i(t) = \begin{cases} \omega_{0i}, & t=0, \\ \omega_r, & 0<t<t_{\text{trap}}, \\ 0, & t>t_{\text{trap}}. \end{cases} \tag{A3}$$

This enables us to calculate the scaling functions b_x and b_y as solutions of Eq. (A2) for the in-trap oscillation. In the limit

of small amplitudes ($\alpha \ll 1$) the solutions are

$$b_x = 1 + \alpha(1 - \cos \omega_q t),$$

$$b_y = 1 - \alpha(1 - \cos \omega_q t), \tag{A4}$$

where $\omega_q = \sqrt{2}\omega_r$ is the radial quadrupole oscillation frequency. Together with Eq. (A1), we are able to determine the difference in widths of the cloud to be

$$\Delta W = -2\alpha W_0 \cos \omega_q t. \tag{A5}$$

2. Dynamic behavior in the collisionless limit

In the collisionless limit, the following set of two uncoupled equations characterizes b_i, where i stands for x,y [43]:

$$\ddot{b}_i = \frac{\omega_{0i}^2}{b_i^3} - b_i \omega_i^2. \tag{A6}$$

In the limit of small amplitudes ($\alpha \ll 1$) solutions of the in-trap oscillation are

$$b_x = 1 + \frac{\alpha}{2}(1 - \cos \omega_q t),$$

$$b_y = 1 - \frac{\alpha}{2}(1 - \cos \omega_q t), \tag{A7}$$

where $\omega_q = 2\omega_r$ is the radial quadrupole oscillation frequency. Together with Eq. (A1), we are able to determine the difference in widths of the cloud to be

$$\Delta W = -\alpha W_0 (1 + \cos \omega_q t). \tag{A8}$$

In contrast to the hydrodynamic limit, the oscillation is initially not centered around $\Delta W = 0$. Furthermore the oscillation has an amplitude 1/2 of the amplitude in the hydrodynamic gas.

Besides the finding of analytical solutions, it is enlightning to understand the collective oscillations in the collisionless limit by considering the phase-space dynamics of the cloud. In Fig. 8, we show the contours of phase-space distributions in the x and y directions. The axes are scaled such that for the round trap—i.e., $\omega_x = \omega_y = \omega_r$—the dynamics of any point in phase-space is a simple circular rotation about the origin with frequency ω_r. Thus, the solid circle in Fig. 8(a) indicates an equilibrium phase-space contour for the round trap. Right after applying the excitation scheme as described in Sec. III the phase-space contours in the x and y directions are given by the dashed and dotted ellipses in Fig. 8(a). Since the gas is fully thermalized at the instant of excitation, the initial momentum distribution in the x and y directions is the same. As time progresses, the elliptic contours will rotate with frequency ω_r [see Fig. 8(b)], which corresponds to oscillations in the trap. We note that both the spatial and momentum distributions in the x direction are never larger than the ones in the y direction. Therefore, ΔW oscillates between $2\alpha W_0$ and zero and the aspect ratio of the cloud never inverts. This is to be compared to the hydrodynamic case where ΔW oscillates between $\pm 2\alpha W_0$.

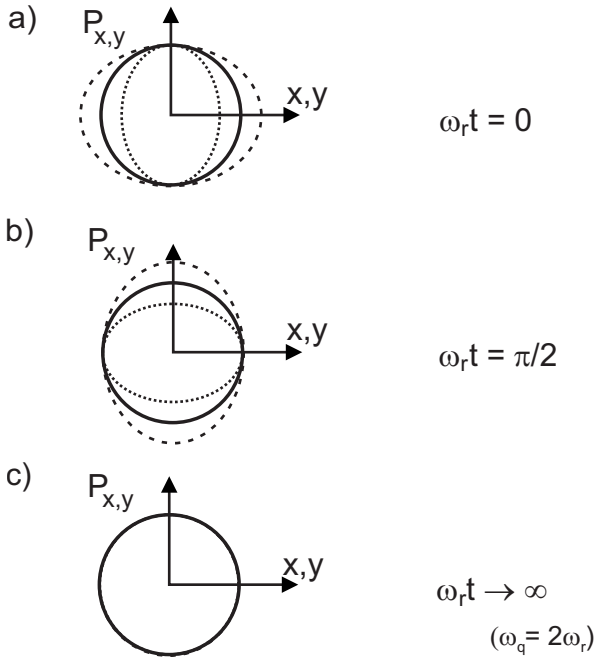

FIG. 8. Phase-space dynamics for the quadrupole mode in the collisionless regime. Shown are phase-space contours of an ensemble of particles which is held in a round trap (i.e., $\omega_x = \omega_y = \omega_r$). In (a) and (b) the situation during the oscillation in the trap is shown for two different times t. The solid line indicates the equilibrium phase-space contour (without excitation), whereas the dotted (dashed) line shows the contour in the x (y) direction after excitation of the oscillation mode. (c) After long times, residual thermalization finally damps out the oscillations and leads to a circular phase space contour.

Residual thermalization effects in a near collisionless gas will damp out the initial oscillation amplitude of αW_0, and one will eventually end up again with a circular phase-space contour [see Fig. 8(c)]. This is studied in detail in Appendix B.

3. Amplitude and phase on expansion

Here we present our calculated results based on the models in Appendixes A 1 and A 2 for the hydrodynamic and collisionless limits, respectively. We show the relative amplitude that is given by the amplitude A [for a definition see Eq. (3)] divided by the average width of the cloud after expansion (for definition details see Sec. IV B). Calculations of this relative amplitude are shown in Fig. 9, whereas calculations and measurements for the phase offset ϕ are shown in Fig. 10.

Figure 9 shows the calculated relative amplitude of a surface-mode oscillation in the hydrodynamic (dashed and dotted curves) and in the collisionless (solid curve) regime as a function of the reduced expansion time $\omega_r t_{TOF}$. The hydrodynamic curves are calculated for the BEC limit of $\gamma = 1$ (upper, dashed curve) and in the unitarity limit of $\gamma = 2/3$ (lower, dotted curve). The amplitude in the collisionless regime is smaller than in the hydrodynamic regime. Initially

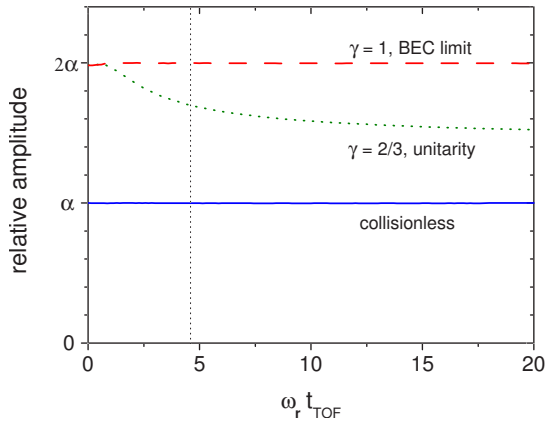

FIG. 9. (Color online) Calculated relative amplitude of a surface mode oscillation versus reduced time of flight $\omega_r t_{\mathrm{TOF}}$ after release from the trapping potential. The values are calculated for the hydrodynamic (dashed curve, $\gamma=1$; dotted curve, $\gamma=2/3$) and collisionless regime (solid curve). The vertical dotted line marks the typical expansion time in our experiments.

the amplitude of the excitation is half as large in the collisionless as in the hydrodynamic regime, as already explained in Appendix A 2. In expansion the normalized amplitude stays constant in the collisionless regime and in the hydrodynamic regime for $\gamma=1$. For $\gamma=2/3$ in the hydrodynamic regime it decreases for longer expansion times.

In Fig. 10 we compare experimental data for the phase shift ϕ with numerical simulations. The data have been taken at unitarity where $1/k_F a=0$ (hydrodynamic, open circles), and on the BCS side of the resonance at $1/k_F a=-1.34$ (collisionless, solid triangles). The dashed line is based on a model for the hydrodynamic interaction regime and the solid line on a model for the collisionless regime. The data agree with the theoretical model where no free fit parameters are used. This confirms our approach presented above.

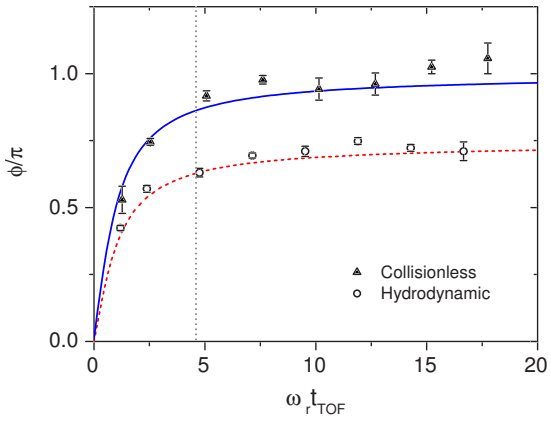

FIG. 10. (Color online) Phase ϕ of the collective surface mode as detected by fits according to Eq. (3) versus reduced expansion time $\omega_r t_{\mathrm{TOF}}$ at unitarity (open circles) and at $1/k_F a=-1.34$ (solid triangles). The lines are numerical simulations for the hydrodynamic (dashed line) and collisionless regime (solid line). The vertical dotted line marks the typical expansion time in our experiments.

APPENDIX B: THERMALIZATION EFFECTS IN A NEAR-COLLISIONLESS GAS

Here we describe thermalization effects in a near-collisionless gas that are not included in the model for the collisionless limit in Appendix A 2. Despite the word "collisionless", collisions play a crucial role for thermalization for our experimental parameters. A typical time scale for thermalization processes is only a few oscillation cycles long. By analyzing the theory, we are able to introduce a universal fit function, as given by Eq. (3), which describes the oscillation both in the hydrodynamic and in the near-collisionless regime.

The measured behavior of the nearly collisionless quadrupole oscillation (see Fig. 4) has two characteristics: after excitation the oscillation is centered around $\Delta W=[W_x(0)-W_y(0)]/2$; then, after some time it is centered around $\Delta W=0$. These two limits are consistent with thermalization of the gas on a relevant time scale greater than the period of the oscillation.

In order to model these effects, we follow a theory based on a classical gas in the transition between the hydrodynamic and the collisionless behavior described in [38]. An application of this theory for the compression mode in the hydrodynamic regime has been used in [41]. Here we will handle thermalization effects of the quadrupole mode in the near-collisionless regime.

Using the classical Boltzmann-Vlasov kinetic equation in the relaxation-time approximation and ignoring mean-field effects one can derive the coupled differential equations [38]

$$\ddot{b}_i = \omega_{0i}^2 \frac{\theta_i}{b_i} - \omega_i^2 b_i \tag{B1}$$

and

$$\dot{\theta}_i = \frac{1}{\tau_R}(\theta_i - \bar{\theta}) - 2\frac{\dot{b}_i}{b_i}\theta_i. \tag{B2}$$

The parameter b_i is the scaling function described earlier in Appendix A, θ_i is a scaling parameter directly related to the temperature, and $\bar{\theta}=\frac{1}{3}\Sigma_k \theta_k$. The initial condition for θ_i is $\theta_i(0)=1$, as long as the gas is in thermal equilibrium at the moment of the excitation. The parameter τ_R is the relaxation time which describes the time scale of collisions. In the collisionless limit, when $\tau_R \to \infty$, the differential equation (B1) simplifies to the simple form in Eq. (A6). For the hydrodynamic limit ($\tau_R \to 0$), we find Eq. (A2).

The solutions to these equations depend on the parameter τ_R as can be seen in Fig. 11. Our measured data in the collisionless regime are well described by $\omega_r \tau_R \sim 2.3$ (compare to Fig. 4).

Universal fit function. We find that the model calculations from Eqs. (B1) and (B2) can be well described by the fit function

$$\Delta W = A e^{-\kappa t_{\mathrm{trap}}} \cos(\omega_q t_{\mathrm{trap}} + \phi) + C e^{-\xi t_{\mathrm{trap}}} + y_0. \tag{B3}$$

The first term describes the exponentially damped oscillations. The second term describes the shift of the center of the

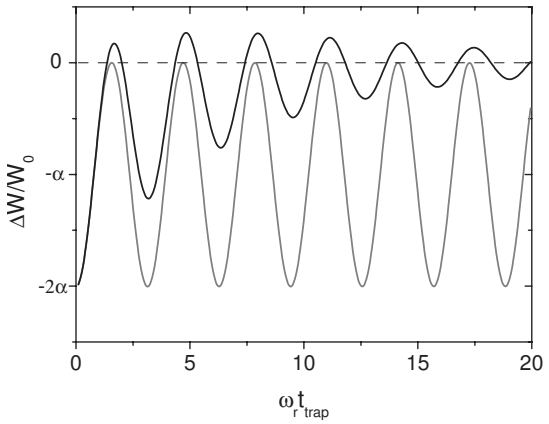

FIG. 11. Calculated quadrupole oscillations in the near-collisionless regime. The lines show the relative difference in width ΔW as a function of the reduced time $\omega_r t_{\mathrm{trap}}$. The oscillation is modeled according to Eqs. (B1) and (B2). The dark line shows the result of the calculation when $\omega_r \tau_R = 2.3$, and the gray line shows the oscillation in the collisionless limit at $\omega_r \tau_R = 1000$.

oscillation in the collisionless regime. The third term y_0 is a constant offset which will be discussed later.

We have used Eq. (B3) to fit our experimental measurements. We find that the free-fit parameters ξ and κ are related through $\xi/\kappa \approx 1.5$ for all our measurements in the near-collisionless regime. In the hydrodynamic regime $C=0$, and therefore ξ becomes irrelevant.

The constant offset y_0 is due to an experimental artifact that results from a slight inhomogeneity of the magnetic field. At the location of the atoms the inhomogeneous magnetic field leads to a weak saddle potential which causes a slight anisotropic expansion during the time of flight. This anisotropy is responsible for a slight offset in ΔW.

APPENDIX C: CORRECTIONS TO THE NORMALIZED FREQUENCY

The theoretical normalized frequencies ω_q/ω_r are calculated for perfectly harmonic trapping potentials in an idealized symmetric trap geometry. There are small derivations from this conditions in real experiments. In order to compare the experimental data to the idealized theoretical case, we have to correct our data. The measured normalized frequency ω_q/ω_r of the radial quadrupole mode has to be increased because of two small corrections. The larger correction is based upon a slight anharmonicity of the trapping potential and the spatial extension of the cloud in the trap. The smaller correction is caused by a small residual ellipticity of the trapping potential.

The potential created by our trapping beam has a Gaussian shape. This results in a nearly harmonic potential in the center of the trap; however, for higher precision one must take into account higher-order terms of the potential. Anharmonicity effects influence both our measurements of the sloshing-mode frequency, where we determine ω_r, and our measurements of the quadrupole-mode frequency ω_q. As we evaluate the normalized frequency ω_q/ω_r, the anharmonicity effects on the sloshing and quadrupole modes almost cancel out each other. The small remaining correction to the normalized frequency is included by multiplying by a prefactor $1+b\sigma$ [20,44]. The anharmonicity parameter σ relates the energy of the oscillation to the total potential depth and is defined by $\sigma = \frac{1}{2} m \omega_r^2 r_{\mathrm{rms}}^2 / V_0$, where r_{rms} is the root-mean-square radius of the trapped cloud and V_0 is the potential depth. The parameter b depends on the interaction regime. In the hydrodynamic regime, it is given by $(4+10\gamma)/(2+7\gamma)$, whereas in the collisionless regime b is determined by $6/5$[44]. Here, γ is the polytropic index of the equation of state. In our experiments, typically $b\sigma \approx 0.014$, but $b\sigma$ can rise to an upper limit of $b\sigma < 0.027$.

In the hydrodynamic regime, there is also a correction due to residual ellipticity effects. This correction takes into account that we compare our measurements with a theory for nonelliptic geometries. The ellipticity ϵ of the trap is defined by $\epsilon = (\omega_y - \omega_x)/\omega_r$. In our experiments, the ellipticity is small and given by $\epsilon \approx 0.07$. Therefore, we can apply the ellipticity correction by multiplication of a prefactor $1+\lambda\epsilon^2$ [20,44], where the interaction dependent factor λ is given by $(\gamma+2)/(4\gamma)$. Altogether, $\lambda\epsilon^2$ is smaller than 0.006 for all data points.

[1] K. M. O'Hara, S. L. Hemmer, M. E. Gehm, S. R. Granade, and J. E. Thomas, Science **298**, 2179 (2002).
[2] T. Bourdel, J. Cubizolles, L. Khaykovich, K. M. F. Magalhães, S. J. J. M. F. Kokkelmans, G. V. Shlyapnikov, and C. Salomon, Phys. Rev. Lett. **91**, 020402 (2003).
[3] S. Jochim, M. Bartenstein, A. Altmeyer, G. Hendl, S. Riedl, C. Chin, J. Hecker Denschlag, and R. Grimm, Science **302**, 2101 (2003).
[4] M. Greiner, C. A. Regal, and D. S. Jin, Nature (London) **426**, 537 (2003).
[5] M. W. Zwierlein, C. A. Stan, C. H. Schunck, S. M. F. Raupach, S. Gupta, Z. Hadzibabic, and W. Ketterle, Phys. Rev. Lett. **91**, 250401 (2003).
[6] C. A. Regal, M. Greiner, and D. S. Jin, Phys. Rev. Lett. **92**, 040403 (2004).
[7] M. W. Zwierlein, C. A. Stan, C. H. Schunck, S. M. F. Raupach, A. J. Kerman, and W. Ketterle, Phys. Rev. Lett. **92**, 120403 (2004).
[8] Ultracold Fermi Gases, Proceedings of the International School of Physics "Enrico Fermi," Course CLXIV, Varenna, 2006, edited by M. Inguscio, W. Ketterle, and C. Salomon (unpublished).
[9] D. M. Eagles, Phys. Rev. **186**, 456 (1969).
[10] A. J. Leggett, *in Modern Trends in the Theory of Condensed Matter*, edited by A. Pekalski and R. Przystawa (Springer Verlag, Berlin, 1980), Vol. 115 of Lecture Notes in Physics, 13.
[11] P. Nozières and S. Schmitt-Rink, J. Low Temp. Phys. **59**, 195 (1985).

[12] J. R. Engelbrecht, M. Randeria, and C. A. R. Sá de Melo, Phys. Rev. B **55**, 15153 (1997).
[13] R. Grimm, in Ultracold Fermi Gases,[8], eprint arXiv:cond-mat/0703091;
[14] J. Cubizolles, T. Bourdel, S. J. J. M. F. Kokkelmans, G. V. Shlyapnikov, and C. Salomon, Phys. Rev. Lett. **91**, 240401 (2003).
[15] S. Jochim, M. Bartenstein, A. Altmeyer, G. Hendl, C. Chin, J. Hecker Denschlag, and R. Grimm, Phys. Rev. Lett. **91**, 240402 (2003).
[16] M. Houbiers, H. T. C. Stoof, W. I. McAlexander, and R. G. Hulet, Phys. Rev. A **57**, R1497 (1998).
[17] M. Bartenstein, A. Altmeyer, S. Riedl, R. Geursen, S. Jochim, C. Chin, J. Hecker Denschlag, R. Grimm, A. Simoni, E. Tiesinga, C. J. Williams, and P. S. Julienne, Phys. Rev. Lett. **94**, 103201 (2005).
[18] J.Kinast, S. L. Hemmer, M. E. Gehm, A. Turlapov, and J. E. Thomas, Phys. Rev. Lett. **92**, 150402 (2004).
[19] M. Bartenstein, A. Altmeyer, S. Riedl, S. Jochim, C. Chin, J. Hecker Denschlag, and R. Grimm, Phys. Rev. Lett. **92**, 203201 (2004).
[20] A. Altmeyer, S. Riedl, C. Kohstall, M. J. Wright, R. Geursen, M. Bartenstein, C. Chin, J. Hecker Denschlag, and R. Grimm, Phys. Rev. Lett. **98**, 040401 (2007).
[21] J. Kinast, A. Turlapov, and J. E. Thomas, Phys. Rev. A **70**, 051401(R) (2004).
[22] J. Kinast, A. Turlapov, and J. E. Thomas, Phys. Rev. Lett. **94**, 170404 (2005).
[23] A. Altmeyer, S. Riedl, C. Kohstall, M. Wright, J. Hecker Denschlag, and R. Grimm, arXiv:cond-mat/0611285.
[24] S. Stringari, Ultracold Fermi Gases in [8]; arXiv:cond/mat/0702526.
[25] C. Chin, M. Bartenstein, A. Altmeyer, S. Riedl, S. Jochim, J. Hecker Denschlag, and R. Grimm, Science **305**, 1128 (2004).
[26] S. Stringari, Phys. Rev. Lett. **77**, 2360 (1996).
[27] R. Onofrio, D.S. Durfee, C. Raman, M. Köhl, C.E. Kuklewicz, and W. Ketterle, Phys. Rev. Lett. **84**, 810 (2000).
[28] V. Bretin, P. Rosenbusch, F. Chevy, G.V. Shlyapnikov, and J. Dalibard, Phys. Rev. Lett. **90**, 100403 (2003).
[29] R. Combescot and X. Leyronas, Phys. Rev. Lett. **93**, 138901 (2004).
[30] R. Combescot, M. Yu. Kagan, and S. Stringari, Phys. Rev. A **74**, 042717 (2006).
[31] M. Bartenstein, A. Altmeyer, S. Riedl, S. Jochim, C. Chin, J. Hecker Denschlag, and R. Grimm, Phys. Rev. Lett. **92**, 120401 (2004).
[32] V. Milner, J. L. Hanssen, W. C. Campbell, and M. G. Raizen, Phys. Rev. Lett. **86**, 1514 (2001).
[33] N. Friedman, A. Kaplan, D. Carasso, and N. Davidson, Phys. Rev. Lett. **86**, 1518 (2001).
[34] We use a periodic modulation with an arcsine-like function. This results in much better harmonic potentials than a simple sawtooth modulation ramp [45].
[35] Ch. Buggle, P. Pedri, W. von Klitzing, and J. T. M. Walraven, Phys. Rev. A **72**, 043610 (2005).
[36] L. Vichi, J. Low Temp. Phys. **121**, 177 (2000).
[37] Note that in the present measurements, the temperatures are somewhat higher than in our recent compression-mode measurements [20]. There are essentially two reasons for the higher temperatures. First, the atoms stay longer in the recompressed trap because of the longer excitation scheme of the quadrupole mode. Second, for the quadrupole measurements we optimized our evaporative cooling scheme regarding particle number and not temperature.
[38] P. Pedri, D. Guéry-Odelin, and S. Stringari, Phys. Rev. A **68**, 043608 (2003).
[39] M. Urban, Phys. Rev. A **75**, 053607 (2007).
[40] Due to the increased Fermi wave number k_F for the deeper trap configuration, the transition in terms of the interaction parameter shifts from $1/k_F a \approx -0.8$ to $1/k_F a \approx -0.5$.
[41] J. Kinast, Ph.D. thesis, Duke University, 2006.
[42] C. Menotti, P. Pedri, and S. Stringari, Phys. Rev. Lett. **89**, 250402 (2002).
[43] G. M. Bruun and C. W. Clark, Phys. Rev. A **61**, 061601(R) (2000).
[44] A. Altmeyer, Ph.D. thesis, University of Innsbruck, 2007.
[45] C. Kohstall, diploma thesis, University of Innsbruck, 2007.